

Constant switching frequency predictive control scheme for three-level inverter-fed sensorless induction motor drive

 D. STANDO^{1,2} and M.P. KAZMIERKOWSKI^{1,2}
¹Electrotechnical Institute, ul. Pożaryskiego 28, 04-703 Warsaw, Poland

²Warsaw University of Technology, ul. Koszykowa 75, 00-662 Warsaw, Poland

Abstract. The paper presents a novel model predictive flux control (MPFC) scheme for three-level inverter-fed sensorless induction motor drive operated in a wide speed region, including field weakening. The novelty of the proposed drive lies in combining in one system a number of new solutions providing important features, among which are: very high dynamics, constant switching frequency, no need to adjust weighting factors in the predictive cost function, adaptive speed and parameter (stator resistance, main inductance) estimation. The theoretical principles of the optimal switching sequence predictive stator flux control (OSS-MPFC) method used are also discussed. The method guarantees constant switching frequency operation of a three-level inverter. For speed estimation, a compensated model reference adaptive system (C-MRAS) was adopted while for IM parameters estimation a Q-MRAS was developed. Simulation and experimental results measured on a 50 kW drive that illustrates operation and performances of the system are presented. The proposed novel solution of a predictive controlled IM drive presents an attractive and complete algorithm/system which only requires the knowledge of nominal IM parameters for proper operation.

Key words: model predictive control (MPC), induction motor (IM), direct torque and flux control (DTFC), sensorless control, MRAS, three-level VSI.

1. Introduction

The model based predictive control (MPC) methods have been recently developed for control in power electronics and drives mainly thanks to advances in digital signal processors (DSP) and field-programmable gate array (FPGA) technologies, allowing to implement even most sophisticated algorithms in real time. Many MPC methods have been developed lately [1–6], however only a few MPC systems are related to the induction motor (IM) drives supplied from three-level inverters [7–12] and, additionally, with speed sensorless operation [13–19].

In this study, we have formulated the following set of practical requirements to facilitate the application of MPC methodology in IM industrial drives and transportation [20]:

- development of a control algorithm operating at inverter constant switching frequency,
- high dynamics of torque control over the entire operating range of the drive, including flux weakening,
- elimination of a speed sensor (increased reliability),
- compensation sensitivity to IM parameters uncertainty.

The research intended to study two groups: the control structure based on the optimal switching sequence (OSS-MPC) (see Fig. 1) and speed/parameter estimation based on the MRAS approach (see Fig. 6). The result of research is an innovative model predictive flux control (OSS-MPFC) method which, in contrast with OSV-MPC, guarantees constant switching frequency of the inverter (Fig. 3). It meets the requirements set,

both in the constant torque region and in the flux weakening region, where in order to increase the torque dynamics it generates dynamic flux weakening. For speed estimation, compensated C-MRAS (Fig. 7) has been proposed, which shows good results in the range from very low speed (10 rpm = 0.5% Ω_{mN}) to high speed in the weakened flux region. Finally, for IM parameters estimation, Q-MRAS (Fig. 11) has been selected. The whole structure (Fig. 3) creates a novel complete predictive control system for IM drive operating in a wide speed range without a mechanical motion sensor.

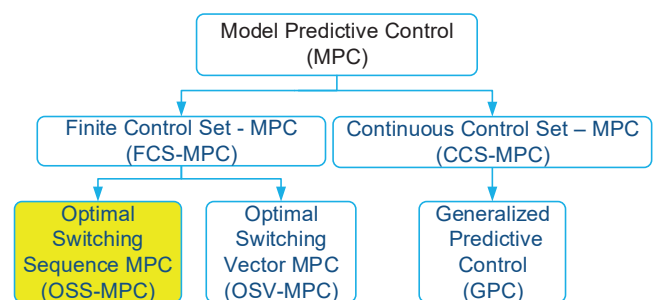


Fig. 1. Placement of the proposed method (yellow) among the MPC group [2]

2. Modelling induction motor and three-level inverter

2.1. Model of IM. The model is based on the cage rotor IM complex space vectors dynamic equation [21, 22]:

$$\mathbf{V}_s = \mathbf{I}_s \cdot R_s + \frac{d\boldsymbol{\Psi}_s}{dt}, \quad (1a)$$

*e-mail: mpk@isep.pw.edu.pl

D. Stando and M.P. Kazmierkowski

$$0 = \mathbf{I}_r \cdot R_r + \frac{d\Psi_r}{dt} - j \cdot p_b \cdot \Omega_m \cdot \Psi_r, \quad (1b)$$

$$\Psi_s = \mathbf{I}_s \cdot L_s + \mathbf{I}_r \cdot L_M, \quad (1c)$$

$$\Psi_r = \mathbf{I}_r \cdot L_r + \mathbf{I}_s \cdot L_M, \quad (1d)$$

$$\frac{d\Omega_m}{dt} = \frac{1}{J} \cdot \left[\frac{3}{2} \cdot p_b \cdot \text{Im}(\Psi_s^* \cdot \mathbf{I}_s) - T_L \right], \quad (1e)$$

where $\mathbf{V}_s = (V_{s\alpha} \ V_{s\beta})$, $\mathbf{I}_s = (I_{s\alpha} \ I_{s\beta})$, $\Psi_s = (\Psi_{s\alpha} \ \Psi_{s\beta})$ are the stator voltage vector, the stator current vector and stator flux vector, respectively. $\mathbf{I}_r = (I_{r\alpha\beta})$, $\Psi_r = (\Psi_{r\alpha\beta})$ are the rotor current vector and rotor flux vector, respectively. Ω_m denotes the rotor electrical angular speed. R_s , R_r , L_s , L_r , L_M are the stator resistance, rotor resistance, stator inductance, rotor inductance and main inductance, respectively. Lastly, p_b denotes the pair of poles, J – the moment of inertia, Ψ_s^* – the conjugate stator flux vector, and T_L is the load torque.

2.2. Model of three-level inverter. Figure 2 depicts the three-phase, three-level neutral point clamped (3L-NPC) voltage source inverter (VSI). Each of the inverter legs can generate

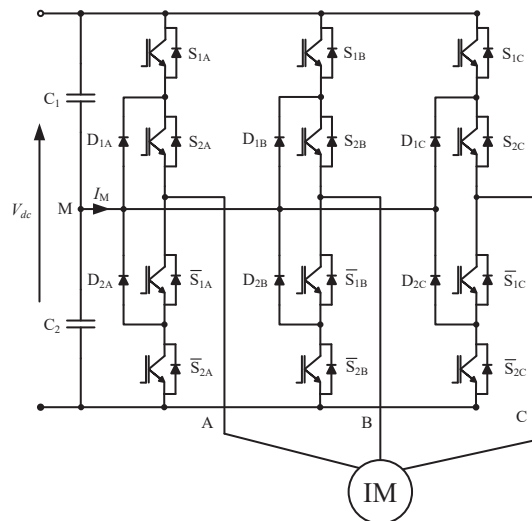


Fig. 2. Circuit of a three-level inverter (top) and representation of output voltage as space vectors and division of the α - β plane into sectors by long vectors and regions by short and medium vectors (bottom)

three voltage levels: $V_{dc}/2$, 0, and $-V_{dc}/2$. This is accomplished by means of three combinations of switch states assigned the number 2, 1 or 0, where: State 2: $V_x = V_{dc}$, State 1: $V_x = V_{dc}/2$, and State 0: $V_x = 0$, for $x = A, B, C$.

Taking into account the available combinations of switch states of individual legs, a three-phase, three-level converter generates 27 basic vectors: 3 zero (000, 111, 222), 12 short (100, 211, 110, 221, 010, 121, 011, 122, 001, 112, 101, 212), 6 medium (210, 120, 021, 012, 102, 201) and 6 long (200, 220, 020, 022, 002, 202) ones.

The state of a given vector is determined in three positions. The first relates to the switches in the leg of phase A, the second to the switches in phase B, the third to the switches in phase C. The switching state vector

$$\mathbf{V}_{ABC} = [V_A, V_B, V_C]^T \in V_{27} := \{000, 001 \dots 221, 222\}. \quad (2)$$

The voltage applied to the IM terminals in orthogonal coordinates $\alpha\beta$ is – for neglected fluctuations of the neutral point potential – given by:

$$\mathbf{V}_{s\alpha\beta} = (V_{dc}/2) \mathbf{K} \mathbf{V}_{ABC}, \quad (3)$$

where \mathbf{K} is reduced Clarke transformation:

$$\mathbf{K} = \frac{2}{3} \begin{Bmatrix} 1 & -\frac{1}{2} & -\frac{1}{2} \\ 0 & \frac{\sqrt{3}}{2} & -\frac{\sqrt{3}}{2} \end{Bmatrix}. \quad (4)$$

3. Predictive stator flux vector control with optimal switching sequence (OSS-MPFC)

The optimal switching sequence-model predictive flux control (OSS-MPFC) control structure developed is implemented in accordance with the algorithm presented in Fig. 3 and Fig. 5. In this system, the control is based on a predictive model and one controller in the form of a cost function with optimization block. In the optimization block, the optimal sector and then the region of inverter voltage plane (Fig. 2) with the reference voltage are selected. Then the switching sequence T_A, T_B, T_C of the three nearest inverter voltage vectors which minimize the cost function (13) are calculated.

3.1. Predictive model. The bases of predictive control are models of the IM and the 3L-VSI. The predictive model of the IM was formulated on basis of the IM equations in a stationary $\alpha\beta$ system (1) transformed into the state equations of the stator flux and current.

$$\frac{d\Psi_s}{dt} = \mathbf{V}_s - R_s \mathbf{I}_s. \quad (5)$$

After transformation using the Euler method, a discrete form of (6) was obtained as:

$$\Psi_s(k+1) = \Psi_s(k) + [\mathbf{V}_s(k) - R_s \mathbf{I}_s(k)] T_s, \quad (6)$$

where: k – sampling step, T_s – sampling time.

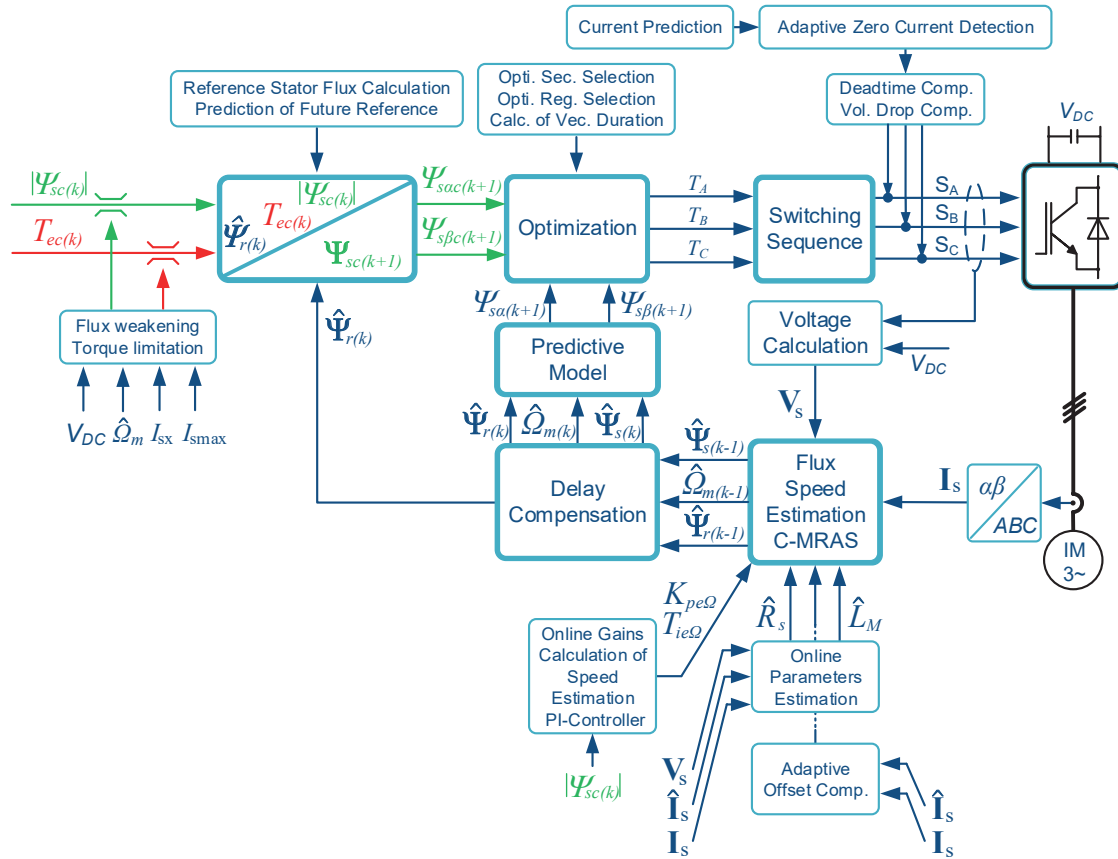


Fig. 3. Full block scheme of the proposed model predictive stator flux control method (OSS-MPFC) with MRAS based speed and IM parameter estimation

Taking into account set (1) one obtains the predictive model of the IM:

$$\Psi_s(k+1) = \Psi_s(k) + \left[\frac{R_r L_m}{\sigma L_s L_r} \Psi_r(k) - \frac{R_s}{\sigma L_s} \Psi_s(k) + \mathbf{V}_s(k) \right] T_s, \quad (7a)$$

$$\Psi_r(k+1) = \Psi_r(k) + \left[\frac{R_r L_s}{L_m} \mathbf{I}_s(k) - \frac{\mathbf{R}_r}{L_m} \Psi_s(k) + \mathbf{j} p_b \mathbf{m} \Psi_r(k) \right] T_s \quad (7b)$$

where $\sigma = 1 - \frac{L_M^2}{L_s L_r}$ is the total leakage factor.

3.2. Cost function and optimization procedure. One of the most important advantages of predictive control is the possibility to use a cost function as a regulator. In the case being discussed, it can be defined as:

$$J = (\Psi_{s\alpha c}(k+1) - \Psi_{s\alpha}(k+1))^2 + (\Psi_{s\beta c}(k+1) - \Psi_{s\beta}(k+1))^2. \quad (8)$$

In this form it is used to determine the optimal sector and then the region. In the first step, the set of stator flux in the $\alpha\beta$ stationary system is determined. For this purpose, the dependence of the phase angle between the stator and rotor flux (so-called

torque angle δ) was used. During no-load operation, the torque angle is equal to zero, whereas when the torque appears on the motor shaft, it is directly proportional to the second component of (10). The first part of (10) results from the currently estimated position of the rotor flux $\gamma_{sr}(k)$. It is also necessary to take into account the effect of prediction, and therefore the desired position of the rotor flux at the application instant of the predicted switch states. This was done according to (9) bearing in mind that the time constant of the rotor circuit is much greater than the stator circuit time constant. Thanks to this, it can be assumed that the increment of the rotor flux angle is the same as in the previous period.

$$\gamma_{sr}(k+1) = \gamma_{sr}(k) + \omega_r T_s \quad (9)$$

$$\gamma_{ssc}(k+1) = \gamma_{sr}(k+1) + \arcsin \left(\frac{2(L_s L_r - L_M^2) T_{ec}(k)}{p_b m_s L_M \Psi_s(k) \Psi_r(k)} \right), \quad (10)$$

$$\Psi_{sc}(k+1) = |\Psi_{sc}(k)| e^{j\gamma_{ssc}(k+1)} \quad (11)$$

this gives the command values of the stator flux $\alpha\beta$ components:

$$\Psi_{s\alpha c}(k+1) = \Psi_{sc} \cos(\gamma_{ssc}(k+1)), \quad (12a)$$

$$\Psi_{s\beta c}(k+1) = \Psi_{sc} \sin(\gamma_{ssc}(k+1)). \quad (12b)$$

In the next step, the optimal sector is set, in which there is a wanted vector minimizing the cost functions. As a result, the number of calculated values of the cost function is reduced from 18 of available vectors (excluding redundant vectors) to only 10. This is accomplished by pre-determining the cost function for the longest vectors, and then finding the minimum sum of the cost functions of two neighboring vectors. Each pair of vectors represents one of the six sectors, as shown in Fig. 2 (bottom). After identifying the optimal sector in the next step, the cost functions are calculated to give the remaining medium and short vectors within it. Then the optimal region is determined, i.e. the one in which the wanted vector is located. This process is similar to the selection of the optimal sector by the force of the fact that in this case a minimum of the sum of three cost functions for neighboring vectors representing the respective regions is sought.

After determining the region in which the voltage vector is located, that we were looking for, we can calculate the switching times of each of the three vectors representing the sector. This is carried out in accordance with the idea presented in Fig. 4 and in Eq. (13).

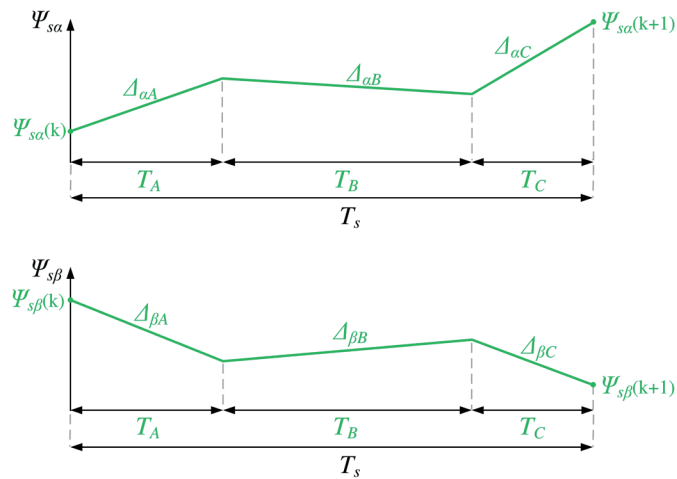


Fig. 4. Changes in the α - β components of the stator flux as a result of the application of three voltage vectors during one sampling period

$$\begin{aligned}
 J = & (\Psi_{s\alpha c(k+1)} - \Psi_{s\alpha(k)} - \Delta_{\alpha A}T_A - \Delta_{\alpha B}T_B \\
 & - \Delta_{\alpha C}(1 - T_A - T_B))^2 \\
 & + (\Psi_{s\beta c(k+1)} - \Psi_{s\beta(k)} - \Delta_{\beta A}T_A - \Delta_{\beta B}T_B \\
 & - \Delta_{\beta C}(1 - T_A - T_B))^2.
 \end{aligned} \quad (13)$$

After calculating partial derivatives with respect to T_A and T_B in accordance with condition (14), we obtain formulas for optimal switching times (15)–(17):

$$\begin{cases} \frac{\partial J}{\partial T_A} = 0, \\ \frac{\partial J}{\partial T_B} = 0, \end{cases} \quad (14)$$

$$\begin{aligned}
 T_A = & \left[(\Psi_{s\alpha c(k+1)} - \Psi_{s\alpha(k)} - \Delta_{\alpha C}) (x_{\alpha AC}x_{\beta BC}^2 - x_{\alpha BC}x_{\beta AC}x_{\beta BC}) \right. \\
 & + (\Psi_{s\beta c(k+1)} - \Psi_{s\beta(k)} - \Delta_{\beta C}) (x_{\beta AC}x_{\alpha BC}^2 \\
 & \left. - x_{\beta BC}x_{\alpha AC}x_{\alpha BC}) \right] / (x_{\alpha AC}x_{\beta BC} - x_{\alpha BC}x_{\beta AC})^2, \quad (15)
 \end{aligned}$$

$$\begin{aligned}
 T_B = & \left[(\Psi_{s\alpha c(k+1)} - \Psi_{s\alpha(k)} - \Delta_{\alpha C}) (x_{\alpha BC}x_{\beta BC}^2 - x_{\alpha BC}x_{\beta AC}x_{\beta BC}) \right. \\
 & + (\Psi_{s\beta c(k+1)} - \Psi_{s\beta(k)} - \Delta_{\beta C}) (x_{\beta AC}x_{\alpha BC}^2 \\
 & \left. - x_{\beta BC}x_{\alpha AC}x_{\alpha BC}) \right] / (x_{\alpha BC}x_{\beta AC} - x_{\alpha AC}x_{\beta BC})^2, \quad (16)
 \end{aligned}$$

where: $x_{\alpha AC} = \Delta_{\alpha A} - \Delta_{\alpha C}$, $x_{\alpha BC} = \Delta_{\alpha B} - \Delta_{\alpha C}$, $x_{\beta AC} = \Delta_{\beta A} - \Delta_{\beta C}$, $x_{\beta BC} = \Delta_{\beta B} - \Delta_{\beta C}$

$$T_C = 1 - T_A - T_B. \quad (17)$$

The flow diagram of the OSS-MPFC algorithm operating with inverter constant switching frequency is shown in Fig. 5.

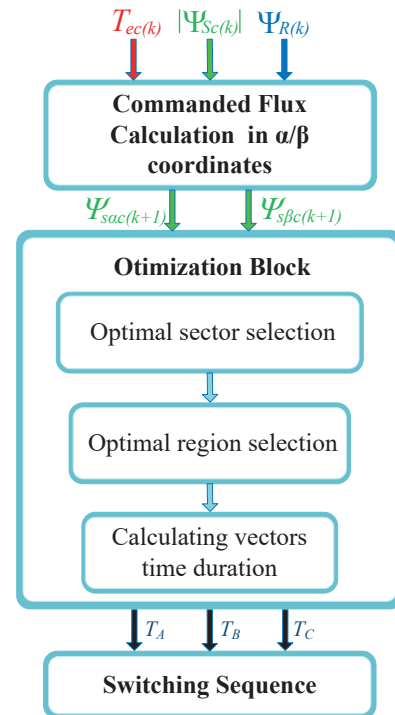


Fig. 5. Flow diagram of the OSS-MPFC algorithm

4. MRAS based speed and IM parameters estimation

To implement vector control of IM, it is necessary to know such directly not measurable state variables as: stator and/or rotor flux, electromagnetic torque and – in sensorless drives – rotor speed/position. Therefore, in recent years a number of state variable estimation methods have been studied and investigated, and among them adaptive systems based on the reference and the adjustable MRAS model (Fig. 6) [23–29] constitute an im-

portant group. The attractiveness of the MRAS methodology results from the fact that it can be used both for estimating speed as well as identifying IM parameters [30–33].

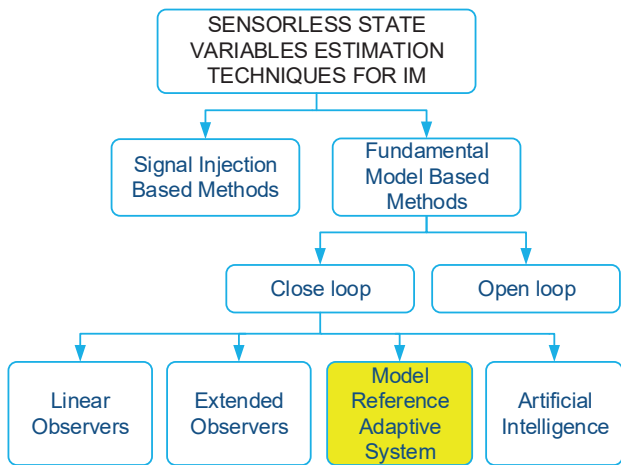


Fig. 6. Classification of IM state variables estimation techniques (MRAS – model reference adaptive system)

4.1. Speed estimation. In this study, the compensated C-MRAS version is used (Fig. 7) [26]. It employs the real IM as the reference model and the full voltage-speed ($V-\Omega_m$) model of the IM [22, 34] as the adaptive model. The C-MRAS, like other variants of MRASs – is parameter-dependent, however it is more robust thanks to real time correction with measured currents.

The adaptive ($V-\Omega_m$) model is derived from the IM model (1) and is described by the following equations:

$$\frac{d\hat{\Psi}_{s\alpha}}{dt} = V_{s\alpha} - R_s \hat{I}_{s\alpha}, \quad (18a)$$

$$\frac{d\hat{\Psi}_{s\beta}}{dt} = V_{s\beta} - R_s \hat{I}_{s\beta}, \quad (18b)$$

$$\frac{d\hat{\Psi}_{r\alpha}}{dt} = \frac{R_r}{L_M} \left(\frac{1}{\sigma} - 1 \right) \hat{\Psi}_{s\alpha} - \frac{1}{\sigma L_r} \hat{\Psi}_{r\alpha} - p_b \hat{\Omega}_m \hat{\Psi}_{r\beta} \quad (19a)$$

$$\frac{d\hat{\Psi}_{r\beta}}{dt} = \frac{R_r}{L_M} \left(\frac{1}{\sigma} - 1 \right) \hat{\Psi}_{s\beta} - \frac{1}{\sigma L_r} \hat{\Psi}_{r\beta} - p_b \hat{\Omega}_m \hat{\Psi}_{r\alpha}, \quad (19b)$$

$$\hat{I}_{s\alpha} = \frac{L_r \hat{\Psi}_{s\alpha} - L_M \hat{\Psi}_{r\alpha}}{\sigma L_s L_r}, \quad (20a)$$

$$\hat{I}_{s\beta} = \frac{L_r \hat{\Psi}_{s\beta} - L_M \hat{\Psi}_{r\beta}}{\sigma L_s L_r}, \quad (20b)$$

where σ is the total leakage factor, and symbol $\hat{}$ denotes estimated values.

As can be seen in Fig. 7, both models are supplied by the same reference voltage \mathbf{V}_s . It is important to consider the delay between the application time and acquisition time. The adaptive system is additionally tuned by two closed loops. The first one considers error between measured current \mathbf{I}_s and calculated form (20), while the second one concerns the adaptively estimated speed (22). The first closed loop is responsible for the compensation of offsets which have the main source in current sensors. The mechanism of offset compensation is realized by two PI controllers, one for each of α, β components. Inputs of these controllers are the current errors ($\mathbf{I}_s - \hat{\mathbf{I}}_s$) while the outputs are the offset compensation signals added to the right side of (18). For the proper compensation in the whole range of the IM rotor speed, the controller time constant is tuned proportionally to the speed value. What is more, the controllers operate very slowly, for two reasons: to ensure lack of influence on the estimation in transients and because they integrate errors from sinusoidal signals. The second closed loop delivers the mechanical speed $\hat{\Omega}_m$ which is estimated based on the error between measured \mathbf{I}_s and estimated $\hat{\mathbf{I}}_s$ currents multiplied by estimated stator flux vector $\hat{\Psi}_s$ according to Eq. (21).

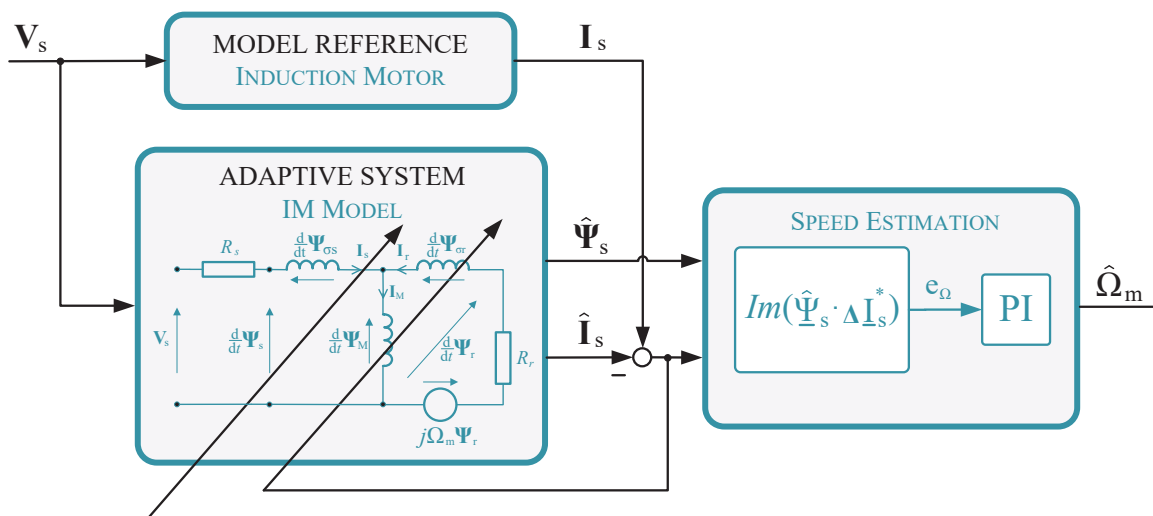


Fig. 7. Block scheme of speed estimation using compensated C-MRAS

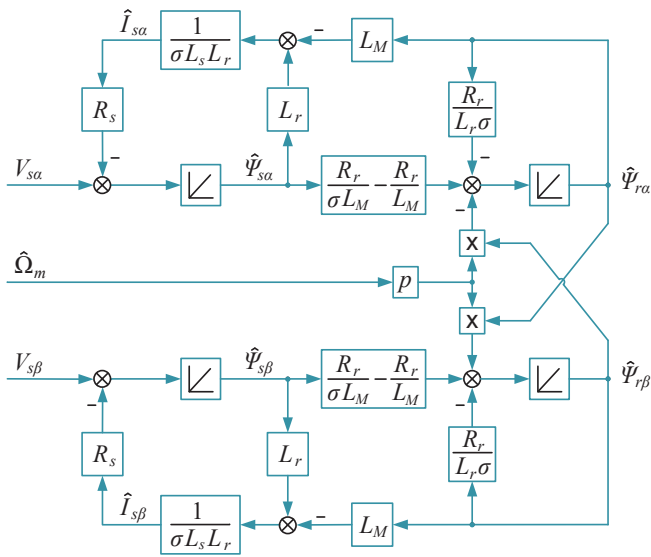


Fig. 8. Voltage-speed flux IM model used as ADAPTIVE SYSTEM (Fig. 7) in C-MRAS

$$e_{\Omega} = \text{Im}(\widehat{\Psi}_s \Delta \widehat{I}_s) = \widehat{\Psi}_{s\beta} (I_{s\alpha} - \widehat{I}_{s\alpha}) - \widehat{\Psi}_{s\alpha} (I_{s\beta} - \widehat{I}_{s\beta}), \quad (21)$$

$$\widehat{\Omega}_m = K_p e_{\Omega} + \frac{K_p}{T_I} \int e_{\Omega} dt. \quad (22)$$

Speed adaptation is performed by the PI regulator (22). This is a fundamental method used for this purpose in MRAS, which ensures intuitive tuning of only two parameters. In the literature, we can also find other mechanisms of speed adaptation, like e.g. ANN [28, 35] or fuzzy logic [10, 36]. In this study, parameters of the PI controller calculated according to the optimum symmetry criterion, using a simplified model of speed estimation loop [20], were set to $K_p = 0.31$ and $T_I = 1.5$ ms. However, in the field weakening region the proportional gain is adapted.

4.2. Influence of parameters uncertainty. A very important criterion characterizing flux/speed estimators is their sensitivity to parameters uncertainty. All algorithmic methods are more or less sensitive to their variation during operation of a drive or their inaccurate identification. There are three main parameters: R_s , R_r and L_M , which influence IM control performance. During standard operation of an IM drive, both stator and rotor windings are heated by the high current flow. This directly impact changes of R_s and R_r , under extreme conditions, even up to 100%. Imprecise knowledge of L_M also has a major impact on the proper operation of the drive. It changes with the state of saturation, according to the magnetization characteristics of the IM. Within the operating range defined by the nominal motor parameters, most drives operate in the linear part of the magnetization characteristic curve. Therefore, the largest changes of L_M occur during operation in the flux weakening region. The presented C-MRAS estimator has been tested by simulation in a steady state of 50 rpm and 1000 rpm speed as well as loads of

0 Nm and 150 Nm. To avoid any negative impact on the properties of the control algorithm in the test, IM was controlled by the actual values from the simulation model and the IM parameters were changed only in the estimator. The changes include: stator (R_s) and rotor resistance (R_r) as well as magnetizing (L_M) and leakage (L_{σ}) inductances in the range of 50% and 150% of the nominal value, where $L_{\sigma} = L_s - L_M = L_r - L_M$. All changes in Figs. 9 and 10 where expressed in pu in percent according to the rules of $\Delta x = \frac{x - \hat{x}}{x} 100\%$ and $\Delta \gamma_s = \frac{\gamma_s - \hat{\gamma}_s}{\pi} 100\%$.

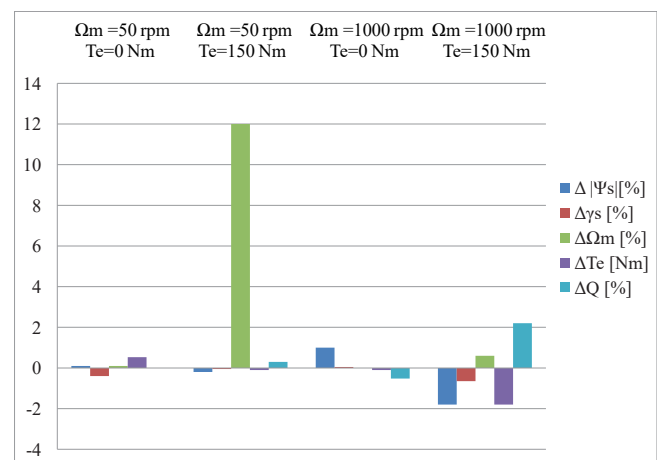
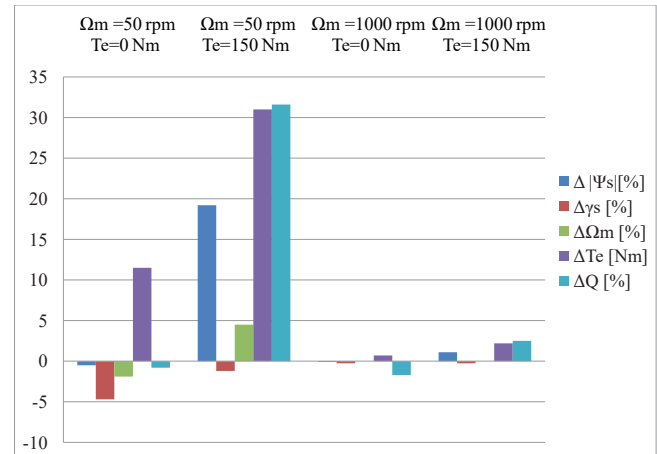
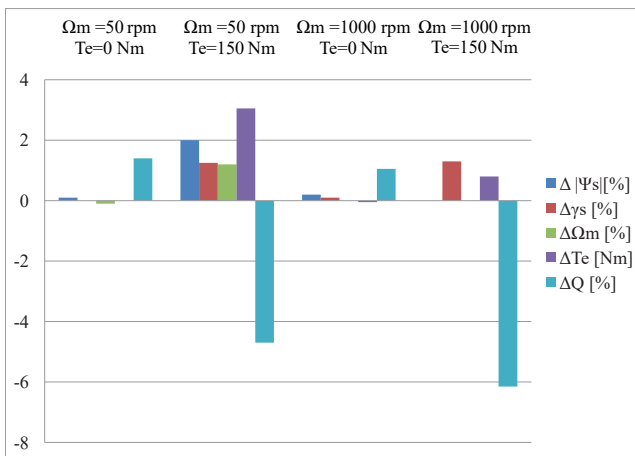
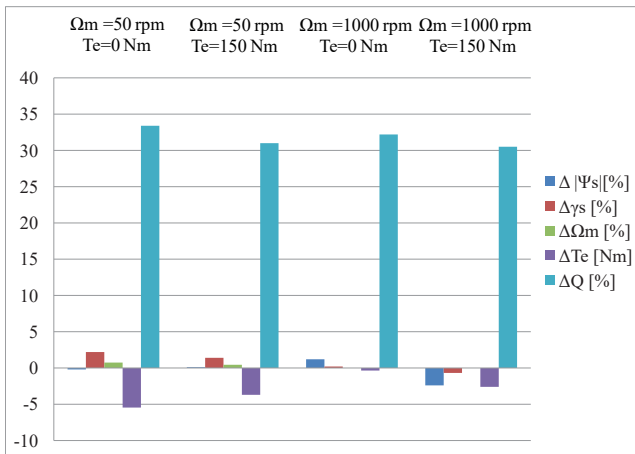


Fig. 9. Influence of 150% R_s (top) and R_r (bottom) uncertainty

As can be seen, most estimation errors are caused by R_s but only in the low speed range where voltage drop on resistance is close to the generated voltage. The errors are visible on all tested variables and increase with increased load. Similarly, the errors generated by R_r are visible in the low speed range. It influences the speed estimation but only when the drive is running under a load, which is visible in Fig. 9. L_M 's greatest impact is noticeable on reactive power, but it also affects flux and torque errors in a similar range as R_s . As the speed increases, the error of investigated variables decreases, except for the reactive power error, which remains at a similar level throughout the whole considered range. It can also be noticed that load changes have no impact on errors generated in this case. The last pa-

Fig. 10. Influence of 150% L_M (top) and L_σ (bottom) uncertainty

parameter L_σ has the least effect on the correct operation of the estimator as compared to other IM parameters and therefore, on-line estimation of L_σ will be not considered.

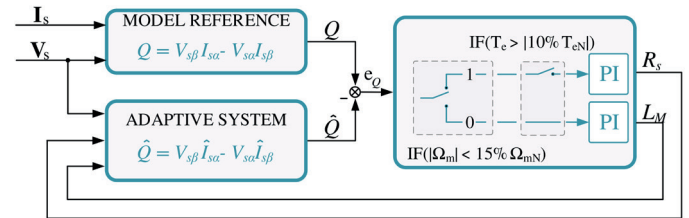
4.3. On-line IM parameters estimation. The analysis presented in the above subsection (Figs. 9 and 10) shows that if \hat{Q} is calculated on the basis of measured voltage and estimated current \hat{I}_s , then it shows strong sensitivity to changes of R_s and L_M . This feature can be used for online estimation of these parameters. Because \hat{Q} differs from Q calculated directly from measured voltage and current, it is possible to formulate the *reference model* (23) and *adaptive system* (24).

$$Q_{ref} = V_{s\beta} I_{s\alpha} - V_{s\alpha} I_{s\beta}, \quad (23)$$

$$\hat{Q}_{ref} = V_{s\beta} \hat{I}_{s\alpha} - V_{s\alpha} \hat{I}_{s\beta}. \quad (24)$$

The greatest flux and torque errors are caused by R_s but only in the low speed range, while L_M influence is significant across the entire speed and torque range. Therefore, it was assumed that a reactive power error e_Q will be used to correct R_s within the range under 15% Ω_m and above 15% Ω_m to correct L_M . It should be noted that incorrect knowledge of L_M in this situation will affect the estimation of R_s . However, it can be assumed that if the initial value of L_M is not burdened by more than a 10%

error, then this fact can be considered insignificant. Moreover, R_s errors will not affect the estimation of L_M . It was also assumed that the limit value above which resistance estimation will be performed is 10% T_{eN} . Figure 11 shows a diagram of the reactive power Q-MRAS estimator.

Fig. 11. Block diagram of R_s and L_M identification using Q-MRAS

As in the case of speed estimation, the PI regulator was also used as an adaptation mechanism in the Q-MRAS estimator. In addition, the direction of rotation and the torque sign had to be taken into account, as the e_Q sign depends on these values. Therefore, the adaptation mechanism is extended to include additional conditions which are listed in Table 1. These relationships are empirically defined. The estimation of R_s depends directly on the speed and torque signs, while the estimation of L_M depends only on the direction of rotation.

Table 1

Influence of mechanical speed and torque direction on R_s and L_M estimation

| L_M | | R_s | | |
|------------|-------|------------|-------|-------|
| Ω_m | e_Q | Ω_m | T_e | e_Q |
| > 0 | $-$ | > 0 | > 0 | $-$ |
| | | | < 0 | $+$ |
| < 0 | $+$ | < 0 | > 0 | $-$ |
| | | | < 0 | $+$ |

The parameter that is not estimated on-line and plays an important role under load is R_r . Due to the fact that it changes under the influence of temperature, like R_s , it is assumed that it will be corrected in proportion to the changes of R_s ($\Delta R_r \approx \Delta R_s$). In addition, the temperature coefficient of the materials used for cage construction can be taken into account.

5. Simulation and experimental results

In this section, because of limited space, only some selected important oscillograms, illustrating operation of the developed IM drive, are presented.

5.1. Flux and torque control dynamics under OSS-MPFC.

The excellent dynamics of stator flux magnitude and torque control illustrate oscillograms in Fig. 12. Additionally, in Fig. 13 the comparison of dynamic performance of the OSS-MPFC and conventional DTC-SVM is presented. Although the prefilter in torque reference path of the DTC-SVM method is

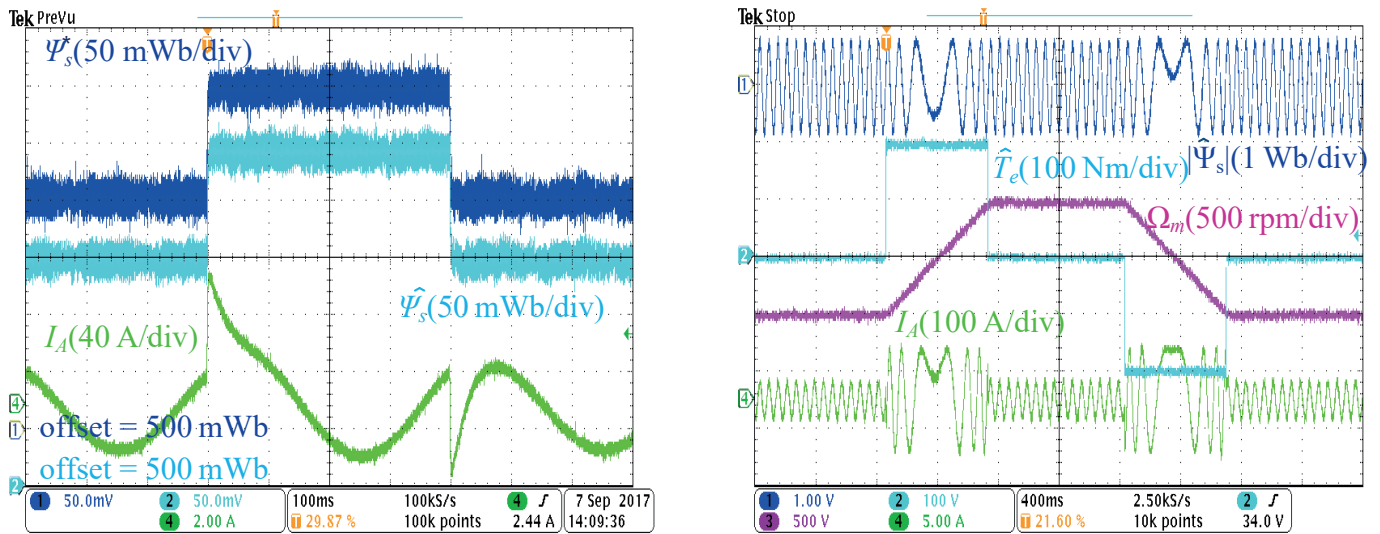


Fig. 12. Dynamic of flux and torque control in OSS-MPTC system. Left: Step in the magnitude of stator flux $0.7 \rightarrow 0.8 \rightarrow 0.7$ Wb: $|\Psi_s^*|$ – reference stator flux, $|\hat{\Psi}_s|$ – estimated stator flux, I_{sa} – phase current. Right: Step in the torque $-200 \rightarrow 200$ Nm: $|\hat{\Psi}_{s\alpha}|$ – estimated stator flux, \hat{T}_e – estimated torque, Ω_m – mechanical speed, I_{sa} – phase current

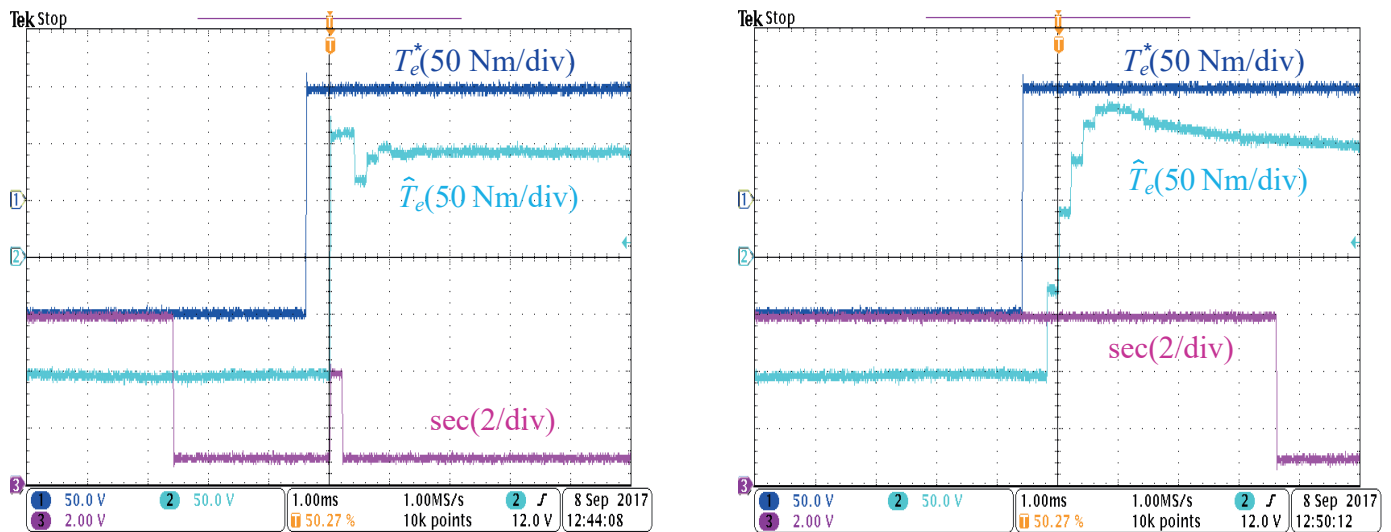


Fig. 13. Comparison of proposed OSS-MPFC (left) and DTC-SVM (right) respond to $-200/200$ Nm commanded torque step T_e^* – commanded torque, \hat{T}_e – torque, sec – voltage sector

disabled, the dynamics of the OSS-MPFC is much better. This is the result of potential generation of the opposite voltage vector, like in the classical DTC [37], which is visible during a temporary change of the inverter voltage sector from 1 to 4 in Fig. 13 (left). In the case of the PI torque controller in the DTC-SVM method, the voltage sector cannot be changed (see Fig. 13 right) or can move only to a neighboring sector, depending on the initial voltage vector's location and proportional controller gain.

5.2. On line R_s and L_M estimation. An example of the process of estimating R_s and L_M parameters is presented in Figs. 14

and 15, respectively. Oscillograms shown at bottom and marked b) and c) are a zoom of the upper part of the oscillograms before and after the starting point of estimation. This makes it possible to observe how the correct knowledge of R_s and L_M affects the current shape. Waveforms of errors in reactive power and mechanical speed are also shown in both figures. Each of them confirms the correct operation of the estimation process because errors of these auxiliary variables were reduced to zero.

5.3. Speed sensorless operation. The test of speed control at slow speed reversal ± 60 rpm during 6 seconds at no-load operation is presented in Fig. 16. The control algorithm passes

Constant switching frequency predictive control scheme for three-level inverter-fed sensorless induction motor drive

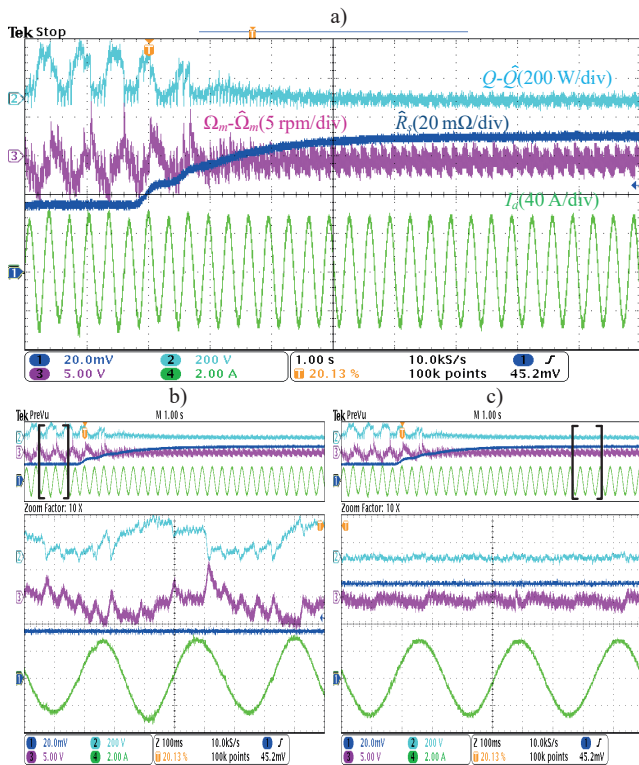


Fig. 14. R_s estimation from 35 m Ω to 71 m Ω at constant -100 rpm and under load torque 10 Nm – generator mode, \hat{R}_s – estimated stator resistance, $Q - \hat{Q}$ – reactive power error, $\Omega_m - \hat{\Omega}_m$ – mechanical speed error, I_A – phase current

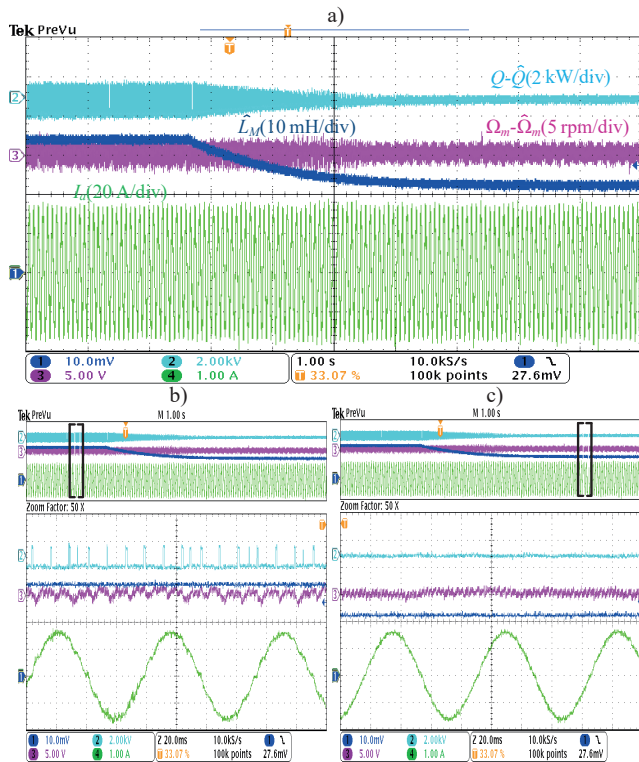


Fig. 15. L_M estimation from 35 mH to 23.4 mH at constant speed 400 rpm and under load torque 110 Nm – motor mode, \hat{L}_M – estimated stator inductance, $Q - \hat{Q}$ – reactive power error, $\Omega_m - \hat{\Omega}_m$ – mechanical speed error, I_A – phase current

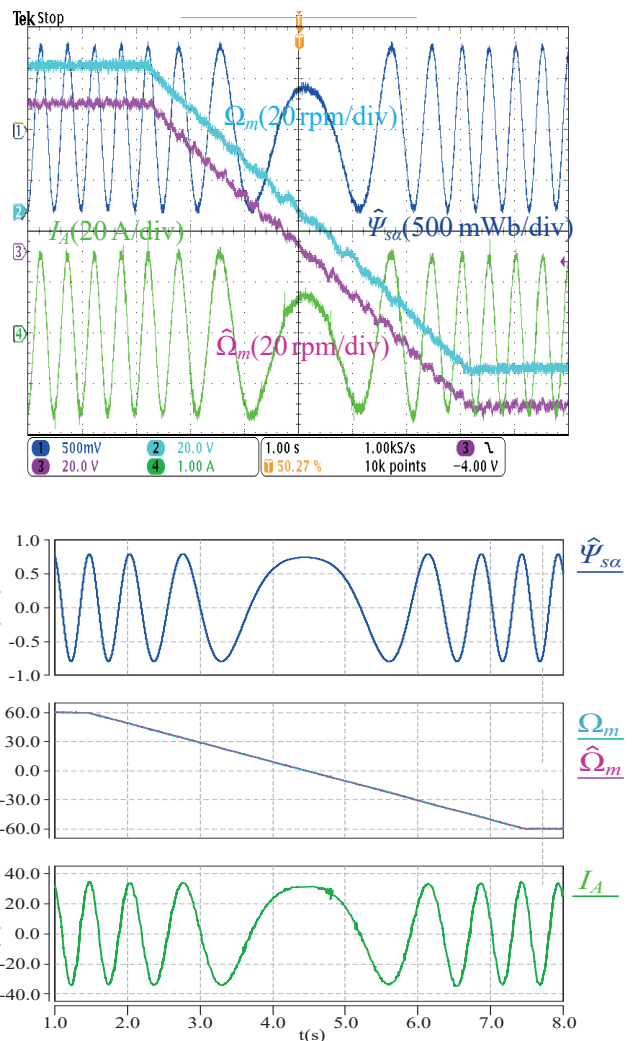


Fig. 16. Sensorless slow speed reversal ± 60 rpm without load torque. Top: experimental; Bottom: simulation. $\hat{\Psi}_{s\alpha}$ – estimated stator flux, Ω_m – measured mechanical speed, $\hat{\Omega}_m$ – estimated mechanical speed, I_A – phase current

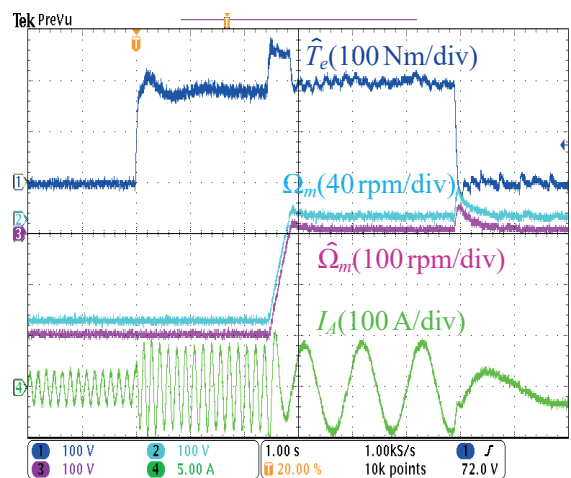


Fig. 17. Sensorless speed reversal from -200 rpm to 10 rpm under 200 Nm load torque, \hat{T}_e – estimated torque, Ω_m – measured mechanical speed, $\hat{\Omega}_m$ – estimated mechanical speed, I_A – phase current

the tests, which is confirmed by good tracking of the measured speed as well as proper shape of the phase current. In Fig. 17 a cycle of speed reversal from -200 rpm to 10 rpm under 200 Nm load torque is shown. Beginning from the left side, the drive works with constant speed of -200 rpm. After two seconds the load of 200 Nm is applied and the IM starts to work as a generator. Next, the commanded speed is set to 10 rpm and the drive changes the mode from generator to motor until the load is switched off in the eighth second.

5.4. Operation in field weakening range. The oscillograms in Fig. 18 show cycles of speed reversal between 1850 rpm and 2250 rpm under ± 170 Nm change of commanded torque. The drive operates with good dynamic and the flux weakening control works properly. It can be noticed that during torque steps the flux is dynamically changed. This is due to the DC-link voltage changes. In the first torque step (170 Nm) the U_{DC} decreases along with the flux magnitude because of increased DC-link current and weak power grid. In the second step (-170 Nm), the drive operates as the generator and decreases the U_{DC} voltage, so the reaction of the flux weakening algorithm is to increase the commanded flux.

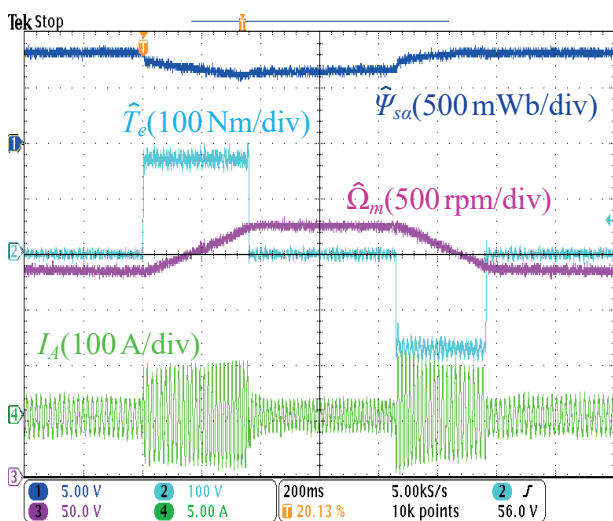


Fig. 18. Reference torque step ± 170 Nm in speed range of $1850/2250$ rpm crossing the boundary of a constant and weakened flux region; \hat{T}_e – estimated torque, $\hat{\Omega}_m$ – measured mechanical speed, $\hat{\Omega}_m$ – estimated mechanical speed, I_A – phase current

Finally, the start-up of the drive up to the field weakening region is shown in Fig. 19. In the field weakening region torque is limited according to the formula including the maximum permitted current [20]:

$$T_{e \max} \leq \frac{3}{2} p_b \Psi_s \sqrt{I_{s \max}^2 - I_{sx}^2} \quad (25)$$

where: I_{sx} – stator magnetizing current.

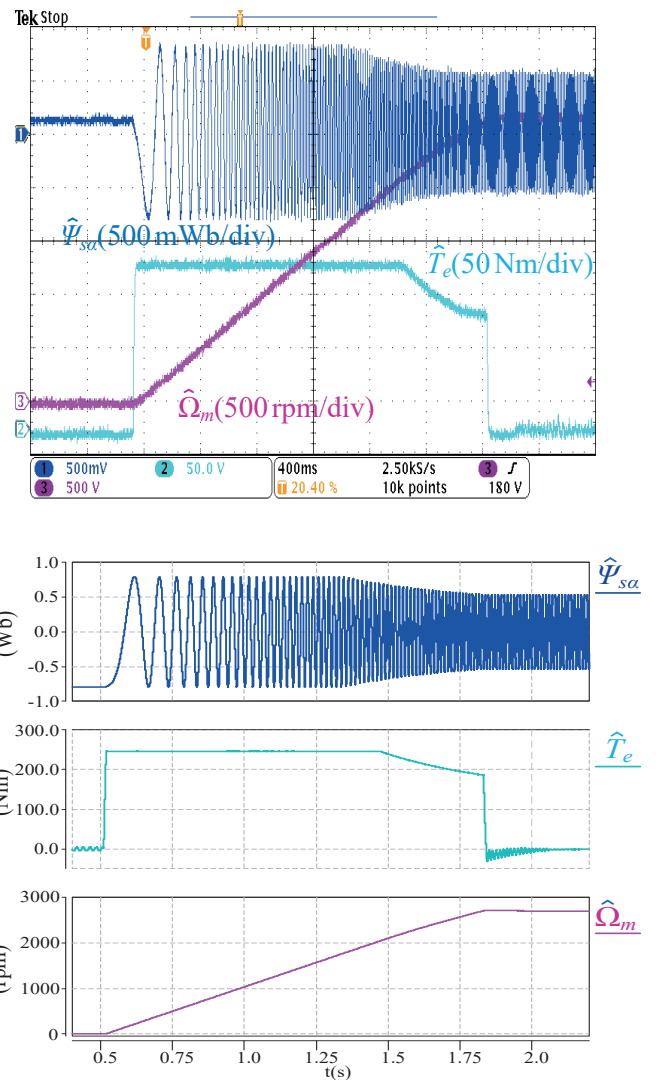


Fig. 19. Start up to 2700 rpm including flux weakening. Top: experimental, Bottom: simulation. $\hat{\Psi}_{s\alpha}$ – estimated stator flux, \hat{T}_e – estimated torque, $\hat{\Omega}_m$ – estimated mechanical speed

6. Conclusions

Main features of the presented model predictive flux controlled (MPFC) scheme for three-level inverter-fed sensorless induction motor drive include:

- very high dynamics; changes of 400 Nm were achieved within just two samplings T_s (see Fig. 13),
- constant inverter switching frequency,
- no need to adjust weighting factors in the predictive cost function, thanks to torque control via direct stator flux adjustment – see (9).
- adaptive speed and parameters (stator resistance, main inductance) estimation, in the range from very low speed (10 rpm = $0.5\% \Omega_{mN}$) to high speed in the flux weakening region.

The theoretical principles of the optimal switching sequence predictive control (OSS-MPFC) used and of the compensated C-MRAS-based estimation methods are discussed. The simu-

lation and experimental results measured on the 50 kW drive, which illustrate operation and performances of the system, are presented.

The proposed novel solution of the predictive controlled IM drive presents an attractive and complete algorithm/system which for proper operation requires only the knowledge of the nominal IM parameters without the necessity of weights factors selection using the “trial and error method”. It also presents methodology of how to combine many innovative solutions in one system to provide excellent, high performance IM drives. In the authors’ opinion, this approach can be used in design of modern drives for industry and transportation.

Appendix

Parameters of the three-level NPC inverter:

$$S_N = 200 \text{ kVA}; \quad I_N = 300 \text{ A}; \quad V_N = 3 \times 400 \text{ V}.$$

Parameters of the IM type STDA 200LU:

$$\begin{aligned} P_N &= 50 \text{ kW}; & V_N &= 3 \times 380 \text{ V}; & I_N &= 88 \text{ A}; \\ f_N &= 65 \text{ Hz}; & T_{eN} &= 249 \text{ Nm}; & p_b &= 2; \\ R_s &= 69.5 \text{ m}\Omega; & R_r &= 46.3 \text{ m}\Omega; & L_s &= 25.217 \text{ mH}; \\ L_r &= 25.137 \text{ mH}; & L_M &= 24.75 \text{ mH}; & J &= 10 \text{ gm}^2. \end{aligned}$$

REFERENCES

- [1] P. Cortés, M.P. Kazmierkowski, R.M. Kennel, D.E. Quevedo, and J. Rodriguez, “Predictive control in power electronics and drives,” *IEEE Trans. Ind. Electron.* 55(12), 4312–4324 (2008), doi: 10.1109/TIE.2008.2007480.
- [2] S. Vazquez, J. Rodriguez, M. Rivera, L.G. Franquelo, and M. Norambuena, “Model Predictive Control for Power Converters and Drives: Advances and Trends,” *IEEE Trans. Ind. Electron.* 64(2), 935–947 (2017), doi: 10.1109/TIE.2016.2625238.
- [3] F. Wang, S. Li, X. Mei, W. Xie, J. Rodríguez, and R. M. Kennel, “Model-based predictive direct control strategies for electrical drives: An experimental evaluation of PTC and PCC methods,” *IEEE Trans. Ind. Informatics* 11(3), 671–681 (2015), doi: 10.1109/TII.2015.2423154.
- [4] F. Wang, Z. Zhang, A. Davari, J. Rodríguez, and R. Kennel, “An experimental assessment of finite-state Predictive Torque Control for electrical drives by considering different online-optimization methods,” *Control Eng. Pract.* 31, 1–8 (2014), doi: 10.1016/j.conengprac.2014.06.004.
- [5] Y. Zhang, B. Zhang, H. Yang, M. Norambuena, and J. Rodriguez, “Generalized sequential model predictive control of im drives with field-weakening ability,” *IEEE Trans. Power Electron.* 34(9), 8944–8955 (2019), doi: 10.1109/TPEL.2018.2886206.
- [6] C. Ionescu and D. Copot, “Hands-on MPC tuning for industrial applications,” *Bull. Pol. Ac.: Tech.* 67(5), 925–945 (2019), doi: 10.24425/bpasts.2019.130877.
- [7] F. Donoso, A. Mora, R. Cardenas, A. Angulo, D. Saez, and M. Rivera, “Finite-Set Model-Predictive Control Strategies for a 3L-NPC Inverter Operating with Fixed Switching Frequency,” *IEEE Trans. Ind. Electron.* 65(5) (2018), doi: 10.1109/TIE.2017.2760840.
- [8] Y. Li, Z. Zhang, and M. P. Kazmierkowski, “Cascaded Predictive Control for Three-Level NPC Power Converter Fed Induction Machine Drives Without Weighting Factors,” in *Proceedings – 2018 IEEE International Power Electronics and Application Conference and Exposition, PEAC 2018*, 2018, doi: 10.1109/PEAC.2018.8590301.
- [9] Y. Zhang and Y. Bai, “Model predictive control of three-level inverter-fed induction motor drives with switching frequency reduction,” in *Proceedings IECON 2017 – 43rd Annual Conference of the IEEE Industrial Electronics Society*, 2017 2017-Janua, pp. 6336–6341, doi: 10.1109/IECON.2017.8217103.
- [10] Y. Zhang, Y. Bai, H. Yang, and B. Zhang, “Low Switching Frequency Model Predictive Control of Three-Level Inverter-Fed im Drives with Speed-Sensorless and Field-Weakening Operations,” *IEEE Trans. Ind. Electron.* 66(6), 4262–4272 (2019), doi: 10.1109/TIE.2018.2868014.
- [11] M. Habibullah, D.D.C. Lu, D. Xiao, and M. F. Rahman, “Finite-State Predictive Torque Control of Induction Motor Supplied from a Three-Level NPC Voltage Source Inverter,” *IEEE Trans. Power Electron.* 32(1), 479–489 (2017), doi: 10.1109/TPEL.2016.2522977.
- [12] S. Aurtenechea, M.A. Rodriguez, E. Oyarbide, and J.R. Torrealday, “Predictive direct power control of MV-grid-connected two-level and, three-level npc converters: experimental results,” in *2007 European Conference on Power Electronics and Applications*, 2007, pp. 1–10, doi: 10.1109/EPE.2007.4417305.
- [13] F. Wang *et al.*, “Encoderless Finite-State Predictive Torque Control for Induction Machine With a Compensated MRAS,” *IEEE Trans. Ind. Informatics* 10(2), 1097–1105 (2014), doi: 10.1109/TII.2013.2287395.
- [14] L. Yan, M. Dou, H. Zhang, and Z. Hua, “Speed-Sensorless Dual Reference Frame Predictive Torque Control for Induction Machines,” *IEEE Trans. Power Electron.* 34(12), 12285–12295 (2019), doi: 10.1109/TPEL.2019.2904542.
- [15] D. Stando, M.P. Kazmierkowski, and P. Chudzik, “Sensorless torque control of induction motor drive operating in wide speed range – Simulation study,” in *16th International Power Electronics and Motion Control Conference and Exposition, PEMC 2014*, 2014, pp. 521–526, doi: 10.1109/EPEPEMC.2014.6980546.
- [16] M. Habibullah, D.D.C. Lu, D. Xiao, J. E. Fletcher, and M.F. Rahman, “Predictive Torque Control of Induction Motor Sensorless Drive Fed by a 3L-NPC Inverter,” *IEEE Trans. Ind. Informatics* 13(1), 60–70 (2017), doi: 10.1109/TII.2016.2603922.
- [17] H. Abu-Rub, D. Stando, and M.P. Kazmierkowski, “Simple speed sensorless DTC-SVM scheme for induction motor drives,” *Bull. Pol. Ac.: Tech.* 61(2), 301–307 (2013), doi: 10.2478/bpasts-2013-0028.
- [18] D. Stando, M.P. Kazmierkowski, T. Orłowska-Kowalska, and M. Dybkowski, “Three selected stator flux vector estimation algorithms for rotor-cage induction motors | Bezczujnikowe sterowanie falownikowego nape{ogonek}du indukcyjnego dla pojazdów elektrycznych w szerokim zakresie prędkości,” *Prz. Elektrotechniczny* 87(3), 307–312 (2011).
- [19] M. Turzyński and P.J. Chrzan, “Resonant DC link inverters for AC motor drive systems – critical evaluation,” *Bull. Pol. Ac.: Tech.* 67(2), 241–252 (2019), doi: 10.24425/bpas.2019.128600.
- [20] D. Stando, *Predictive Control of 3-Level Inverter-Fed Sensorless Induction Motor Drive*, PhD Thesis. Warsaw: Warsaw University of Technology, Faculty of Electrical Engineering, 2018.
- [21] M.P. Kazmierkowski, R. Krishnan, and F. Blaabjerg, *Control in Power Electronics: Selected Problems*. 2003.

- [22] M.P. Kazmierkowski and H. Tunia, *Automatic Control of Converter-Fed Drives*. Amsterdam-London-New York-Tokyo, Warsaw: Elsevier Ltd, 1994.
- [23] C. Schauder, "Adaptive Speed Identification for Vector Control of Induction Motors Without Rotational Transducers," *IEEE Trans. Ind. Appl.* 28(5), 1054–1061 (1992), doi: 10.1109/28.158829.
- [24] G. Tarchala, M. Dybkowski, and T. Orłowska-Kowalska, "Analysis of the chosen speed and flux estimators for sensorless induction motor drive," *2011 IEEE International Symposium on Industrial Electronics*, Gdansk, 2011, pp. 525–530, doi: 10.1109/ISIE.2011.5984213.
- [25] G. Tarchala and T. Orłowska-Kowalska, "Equivalent-Signal-Based Sliding Mode Speed MRAS-Type Estimator for Induction Motor Drive Stable in the Regenerating Mode," *IEEE Trans. Ind. Electron.* 65(9), 6936–6947 (2018), doi: 10.1109/TIE.2018.2795518.
- [26] T. Orłowska-Kowalska and M. Dybkowski, "Stator-current-based MRAS estimator for a wide range speed-sensorless induction-motor drive," *IEEE Trans. Ind. Electron.* 57(4), 1296–1308 (2010), doi: 10.1109/TIE.2009.2031134.
- [27] A.V. Ravi Teja, C. Chakraborty, S. Maiti, and Y. Hori, "A new model reference adaptive controller for four quadrant vector controlled induction motor drives," *IEEE Trans. Ind. Electron.* 59(10), 3757–3767 (2012), doi: 10.1109/TIE.2011.2164769.
- [28] S. Maiti, V. Verma, C. Chakraborty, and Y. Hori, "An adaptive speed sensorless induction motor drive with artificial neural network for stability enhancement," *IEEE Trans. Ind. Informatics* 8(4), 757–766 (2012), doi: 10.1109/TII.2012.2210229.
- [29] I. Benlaloui, S. Drid, L. Chrifi-Alaoui, and M. Ouriagli, "Implementation of a new MRAS speed sensorless vector control of induction machine," *IEEE Trans. Energy Convers.* 30(2), 588–595 (2015), doi: 10.1109/TEC.2014.2366473.
- [30] L. Zhen and L. Xu, "Sensorless field orientation control of induction machines based on a mutual MRAS scheme," *IEEE Trans. Ind. Electron.* 45(5), 824–831 (1998), doi: 10.1109/41.720340.
- [31] A.V. Ravi Teja, V. Verma, and C. Chakraborty, "A New Formulation of Reactive-Power-Based Model Reference Adaptive System for Sensorless Induction Motor Drive," *IEEE Trans. Ind. Electron.* 62(11), 6797–6808 (2015), doi: 10.1109/TIE.2015.2432105.
- [32] S.A. Davari, F. Wang, and R.M. Kennel, "Robust Deadbeat Control of an Induction Motor by Stable MRAS Speed and Stator Estimation," *IEEE Trans. Ind. Informatics* 14(1), 200–209 (2018), doi: 10.1109/TII.2017.2756900.
- [33] V.V. Vasić and S.N. Vukosavić, "Sensorless MRAS-based induction motor control with parallel speed and stator resistance estimation," *Eur. Trans. Electr. Power* 12(2), 135–139 (2002), doi: 10.1002/etep.4450120208.
- [34] M. Depenbrock, "Direct Self-Control (DSC) of Inverter-Fed Induction Machine," *IEEE Trans. Power Electron.* 3(4), 420–429 (1988), doi: 10.1109/63.17963.
- [35] S.M. Gadoue, D. Giaouris, and J. W. Finch, "Sensorless control of induction motor drives at very low and zero speeds using neural network flux observers," *IEEE Trans. Ind. Electron.* 56(8), 3029–3039 (2009), doi: 10.1109/TIE.2009.2024665.
- [36] M. Dybkowski and T. Orłowska-Kowalska, "Low-speed performance of the stator current-based MRAS estimator with FL controller in the sensorless induction motor drive," in *11th International Conference on Optimization of Electrical and Electronic Equipment, OPTIM 2008*, 2008, pp. 75–80, doi: 10.1109/OPTIM.2008.4602460.
- [37] G.S. Buja and M.P. Kazmierkowski, "Direct torque control of PWM inverter-fed AC motors – A survey," *IEEE Trans. Ind. Electron.* 51(4), 744–757 (2004), doi: 10.1109/TIE.2004.831717.